

Spatial Distribution of Primary Radiation Damage in Microstructures

Patrick Burr (✉ p.burr@unsw.edu.au)

The University of New South Wales <https://orcid.org/0000-0003-4796-9110>

Matthew Brand

The University of New South Wales

Edward Obbard

The University of New South Wales

Article

Keywords: primary radiation damage, damage localisation, NRT theory, BCA simulations

Posted Date: July 20th, 2022

DOI: <https://doi.org/10.21203/rs.3.rs-1848790/v1>

License:  This work is licensed under a Creative Commons Attribution 4.0 International License.

[Read Full License](#)

Spatial Distribution of Primary Radiation Damage in Microstructures

M.I. Brand^a, E.G. Obbard^a, P.A. Burr^a

^a*School of Mechanical and Manufacturing Engineering, The University of New South Wales, Sydney, 2052, NSW, Australia*

Abstract

The universally-used theory of Norgett, Robinson and Torrens (NRT) for calculating primary radiation damage in materials assumes that materials are homogeneous. For many engineering materials, which have rich microstructures, this assumption is poor. As there are no alternative radiation damage theories that include heterogeneity, the role of the microstructure on primary radiation damage has been neglected, and assumed to only affect defect recombination (as opposed to production). Here we extend the NRT formalism to account for microstructural variations and account for the damage caused in a phase by primary knock-on atoms that are produced in another nearby phase. The new approach converges to conventional NRT at suitably large length-scales, and agrees with binary collision approximation simulations for individual phases of a microstructure. Applying the method to a ferritic superalloy, we show that there is substantial spatial variation of primary radiation damage (up to 30% from one phase to another, and up to 7% within a single phase), and that the damage is localised in the ferrite matrix and not the precipitates, which is the opposite of what is predicted by macro-

Email address: p.burr@unsw.edu.au (P.A. Burr)

scopic approaches. Substantially greater localisation of damage is predicted for more chemically heterogeneous materials. Our new approach provides new physical insight into the interplay between microstructure and primary radiation damage.

Keywords: primary radiation damage, damage localisation, NRT theory, BCA simulations

1. Introduction

Materials that are subject to high energy radiation undergo changes in their atomic structure, which then evolve into larger microstructural defects, often with detrimental changes to the material properties. Thus, understanding radiation-matter interaction is of paramount importance in advancing materials for a range of applications, from nuclear energy and nuclear technologies to outer space and radio-pharmaceutical production.

When a high energy neutron interacts with a material, it displaces an atom from its original site in the crystal lattice. These displaced atoms are known as the primary knock-on atoms, or PKAs, which then go on to create subsequent cascades of atomic collisions. In this sense, the damage is not directly caused by neutron collisions, but by the interaction and stopping of PKAs displacing further atoms within the material. The total number of displacements per atom (dpa) is a common metric of the primary radiation damage in the material [1]. While many of the defects created by these displacements annihilate within pico-seconds of the collision event, residual defects are left behind, and their accumulation and evolution leads to range of material-specific radiation effects, such as swelling, embrittlement, growth,

19 chemical segregation and enhanced corrosion [2, 3].

20 Methods to calculate the damage that neutrons cause to a material have
21 been developed since the 1940's [4], and fall into one of two categories: analyt-
22 ical coarse-grained methods, such as the Kinchin-Pease [5, 6] and NRT [7, 8]
23 models; and explicit atomic-scale simulations such as molecular dynamics
24 and Monte Carlo simulations. While the former are fast and yield useful
25 values for engineering application, they do so by approximating the material
26 as an amorphous solid of homogeneous composition. For most engineering
27 materials, this assumption is often inadequate. This is especially true when
28 the mean free path of PKAs is in the range of nano- to micro-meters [9],
29 which is commensurate with that of engineering materials' microstructures.
30 On the other hand, atomic-scale simulations provide an accurate descrip-
31 tion of the collision cascade event, with pico-meter and femto-second resolu-
32 tion, but they are too costly to extend beyond nano-meter length scale and
33 nano-second timescale. Thus, neither approach can provide information of
34 radiation damage at the microstructural length scale. This has led to the de-
35 velopment of multi-scale approaches [10, 11], which feed the results of atomic
36 scale simulations into larger scale models e.g., discrete dislocation dynamics,
37 phase field modeling, kinetic Monte Carlo, or rate theory. However, these are
38 still computationally intensive approaches that require significant user input
39 and development.

40 One way to fulfill this gap, is to consider each constituent phase of a
41 material as separate bulk phases, and perform NRT calculations on each
42 phase separately. While this technique has provided novel insight in selected
43 cases [12], it assumes that all damage within a phase is caused by PKAs

44 generated in that same phase, and that PKAs of one material do not con-
45 tribute to damage in another phase, which is unphysical. This approach is
46 only appropriate when the phases are much larger than the mean free path
47 of the PKAs. As we show in this paper, this approach can lead to significant
48 errors, even qualitatively wrong answers, for some engineering alloys.

49 When damage is caused by ions rather than neutrons, it can be accurately
50 modelled using binary collision approximation (BCA) simulations, such as
51 the commonly used SRIM/TRIM packages[13, 14]. BCA uses a Monte Carlo
52 algorithm to calculate the ion passage, deposition and collision cascade dis-
53 placements within the material [7, 13, 14, 15, 16]. BCA calculations have the
54 appropriate length and time scales to account for micro-structural features
55 and are a promising technique to bridge the gap in methodology to study
56 spatial distribution of damage in heterogeneous microstructure. However,
57 there is no established method to integrate the interaction between radiation
58 and microstructural features within the BCA formalism.

59 The nuclear industry routinely adopts the NRT formulation because its
60 simplicity allows for a like-for-like comparison when investigating new mate-
61 rials or new radiation conditions [17]. However, the limitations of the NRT
62 method are important, particularly for modern superalloys, composites and
63 hybrid materials. Here we expand the NRT formulation, to account for spa-
64 tial heterogeneities. We do so by combining both BCA and NRT theories
65 to quantify the degree of localisation and spatial distribution of primary
66 radiation damage production in materials with arbitrarily heterogeneous mi-
67 crostructures. In Section 2 we present an overview of the theoretical frame-
68 work to expand the NRT model, with further details provided in the meth-

69 ods section and supplementary information. Section 3 then demonstrates the
70 method through case studies, and investigates over what length scales the
71 method is superior to the approximation of a homogeneous material.

72 **2. Theoretical Framework**

73 Our approach aims to extend the NRT formulation to include the in-
74 terplay between microstructural heterogenities and primary radiation dam-
75 age generation. In the limit of a homogeneous distribution of species, our
76 method must collapse into the analytical NRT solution. We will show that
77 in the limit of macroscopic, distribution of constituent phases (i.e. grains
78 larger than PKA’s mean free path) the method also collapses into the NRT
79 solutions applied to each phase individually.

80 The NRT model separates primary damage into two processes: first the
81 incident neutron flux (ϕ_N) interacts with the material to produce a PKA flux
82 (ϕ_{PKA}), according to known interaction cross-sections [18, 19, 20]. Second,
83 the PKAs travel through the material causing further displacements. Tradi-
84 tional NRT theory uses the Lindhard-Scharff-Schiott (LSS) theory [21, 22, 23]
85 to determine the portion of the PKA energy that displaces atoms in a bulk
86 material [8]. Alternatively, this energy can be calculated from BCA simula-
87 tions which describes the energy imparted to the material by the PKA as a
88 function of depth [14]. In principle the total damage produced by a neutron
89 flux can be calculated with a set of BCA simulations: one set for every PKA
90 species and for every PKA energy that is created by the neutron flux, with
91 the results summed and weighted accordingly [24, 25]. For a homogeneous
92 single-phase material, this is a large but feasible set of calculations.

93 To apply this approach to heterogeneous microstructures, one must con-
 94 sider that the PKAs will cross the interface between two different phases.
 95 The damage produced in a uniform small volume of material (a target voxel)
 96 is caused by all PKAs generated in all other (source) voxels within a sphere
 97 of radius $|r - r_0|$ as shown schematically in Figure 1. Some of these voxels
 98 may reside in a different phase, and across one or more interfaces.

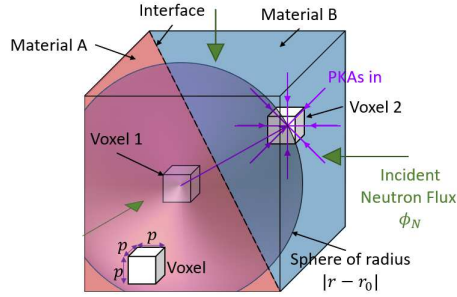


Figure 1: Schematic of the primary radiation damage process in a volume of heterogeneous material subject to a neutron flux ϕ_N . Every region of space (voxel 1) yields a PKA flux which travels and creates damage in other regions of the material that lie within a given radius. One such voxel in that range is highlighted (voxel 2), in this case residing across an interface in another phase.

Mathematically, we describe the damage K as

$$K = \sum_{r_0} \sum_{E_0} S(E_0)F(r_0)f(r_0, E_0) \quad (1)$$

99 where S is the number of PKAs generated isotropically at the source voxel
 100 given a neutron flux ϕ_N , F is the fraction of those PKAs whose path in-
 101 tersect the target voxel, and f is the damage per ion that the target voxel
 102 experiences due to those PKAs. S is obtained by interrogating databases of
 103 known nuclear interaction cross-sections (see Methods); F is derived deter-
 104 ministically using a geometric argument presented in the Methods section,

105 however, it could also be calculated through statistical sampling. f is not
106 known *a-priori*. In principle f could be calculated explicitly from a large
107 set of BCA simulations, if these were repeated with statistical significance
108 for each PKA species, PKA energy, source location, source direction and in-
109 terface distance. This is computationally intractable for any geometry more
110 complex than an infinite planar 2D interface. We propose a computationally
111 efficient and accurate way to reduce the parameter space, which results in an
112 analytical description of f . An overview is provided below, and a detailed
113 derivation is given in the Methods section. In the result section, this is vali-
114 dated against a set of explicit BCA calculations for simple planar interfaces
115 (section 3.1) before applying it to solve Eq. (1) for arbitrary (section 3.2)
116 and realistic (section 3.3) microstructures.

117 The parameter space of f was reduced by removing the interface distances
118 as a simulation parameter and predict damage profiles from the BCA damage
119 profiles of the constituent (bulk) phases. Damage in a single phase is defined
120 as a function of the PKA energy, and fitted to a continuous function that
121 is consistent with LSS theory [21, 22, 23, 26]. The function is linear in the
122 limit of the electronic stopping regime and is a power-law in the limit of
123 the nuclear stopping regime. The damage profile across an interface is then
124 taken by splicing the (fitted) damage profiles of the constituent bulk phases,
125 such that the PKA energy is continuous. This means the damage profile is
126 not a continuous function of the distance, but is a continuous function of
127 PKA energy. This is illustrated schematically in Figure 2, where a PKA
128 creates two different damage profiles (represented by the ovals) in the two
129 materials (left and right). Each damage profile has a characteristic range

130 (length of oval) and magnitude of damage (width of oval), and the PKA
 131 reaches given energies E_1 and E_2 at two different distances. In a composite
 132 material (central cartoon), the damage is approximated by the damage that
 133 the same PKA creates in the constituent bulk phases when it has the same
 energy, which may not be at the same distance.

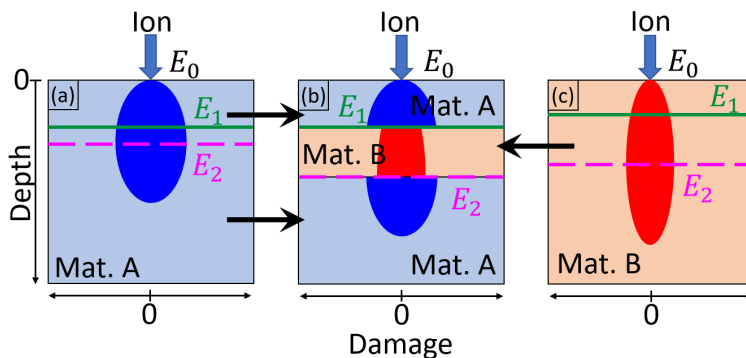


Figure 2: Graphical representation of radiation damage mechanism across material interfaces. Blue indicates material A and orange indicates material B. Ovals indicate the displacement cascade within the material, where the width of oval represents the magnitude of displacements and the length represents the depth at which displacements occur. The horizontal lines represent the distance in the different materials at which the PKA reaches a specific energy. (a) and (c) show the damage profile in pure materials. (b) shows the damage profile in the composite material.

134

135 3. Results

136 3.1. Method validation

137 For validation we compare the predictions from the current method to
 138 explicit BCA calculations of damage profile across a planar interface for a
 139 range of PKA initial energies, material compositions, and interface distance.

140 Figure 3 shows two characteristic examples of such radiation damage profiles,
 141 where the black line is the explicit BCA simulation, and the coloured lines
 142 are from the proposed approximation. In the example, a 100 keV Fe ion
 143 crosses an interface at 20 nm between Fe and Al layers. Other examples can
 144 be found in the supplementary information.

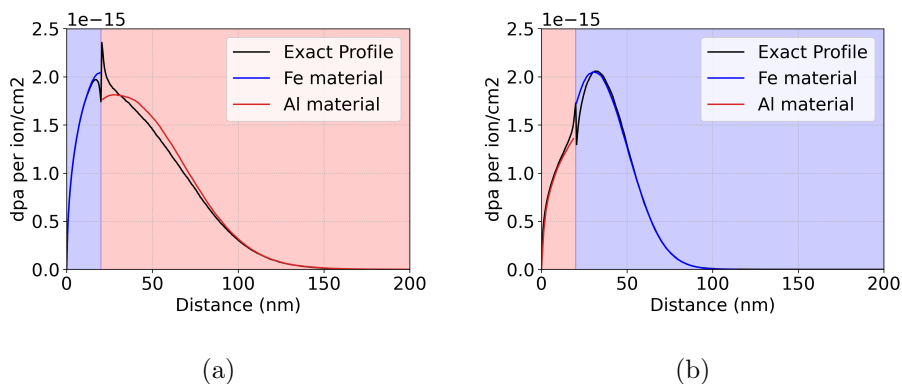


Figure 3: The damage profile of a 100 keV Fe ion across an (a) Fe-Al interface and (b) Al-Fe interface at 20 nm from the surface. Black line shows the exact profile, calculated with explicit BCA simulations of the layered materials. Coloured lines show the predicted damage of the novel method, using Eq. (13). Shading represents the composition of the materials (red=Al, blue=Fe)

145 The novel method (coloured lines) of using the damage profiles in con-
 146 stituent phases is in good agreement with the explicit BCA simulation of
 147 the composite structure (black line). There is a sharp discontinuity at the
 148 interface of the explicit calculation due to the sudden change in threshold
 149 displacement energy, E_d , and cascade chemical composition. This effect is
 150 discussed in greater detail in later sections. While the novel method does
 151 not capture the exact profile at the discontinuity, the agreement is excellent

152 beyond a few nano-meters from the interface, where the cascade particles of
153 the neighbouring phase have come to rest and all new damage is caused by
154 particles of same chemistry as the phase in which they travel.

155 To evaluate the accuracy of the method, we consider the root mean square
156 error (RMSE) of the damage calculated by the proposed method, against that
157 of explicit BCA simulations, for several scenarios in which a PKA crosses an
158 interface located at different depths, shown in Figure 4. It is evident that
159 the total RMSE (solid lines) is below 5% for most interface depths, and
160 can be as low as 2% when the interface from Fe to Al layers is at <10 nm
161 or >200 nm. If one discounts the region in the immediate vicinity of the
162 interface (± 10 nm) and recalculates the RMSE for the rest of the damage
163 curve, the agreement improves remarkably (dotted lines). This indicates
164 that the discrepancy between our model and the explicit BCA calculations
165 is chiefly due to the discontinuity at the interface itself, and the model cor-
166 rectly captures the propagation of damage in the bulk of a phase when the
167 PKAs originated in a different phase, to within a few percent. This provides
168 confidence in using our analytical formulation to perform high-throughput
169 calculations across arbitrary interfaces.

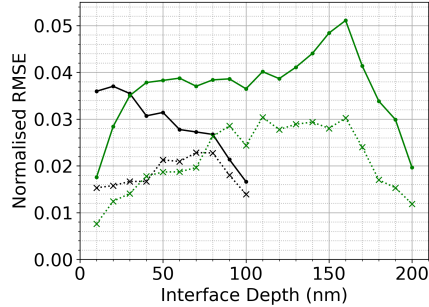


Figure 4: RMSE, normalised by the maximum value, of the damage profile generated by the novel method compared to the exact profile due to a 200 keV Fe ion moving from Fe to Al (Black line) and from Al to Fe (Green line). The solid line shows the RMSE from the full profile, while the dotted line shows the RMSE when the region ± 10 nm from the interface is excluded.

170 In essence, the method predicts the radiation damage profile by a PKA
 171 (or any ion) in a multi-phase material/composite using only the damage and
 172 energy profiles of the PKA in the constituent phases. One direct application
 173 of the method is in parametric studies of ion irradiation of layered mate-
 174 rials. Greater benefit becomes apparent when investigating more complex
 175 2D and 3D microstructures, which would not be feasible using explicit BCA
 176 calculations.

177 3.2. Application to a model microstructure

178 Figure 5 shows an example application of the method using Eq. (1),
 179 applied to an idealised 2D microstructure containing a circular particle of
 180 W/Mg (white phase) with radius 50 nm embedded in a matrix of Al/Fe
 181 (black phase). The top half of the figure shows the microstructure, while the
 182 bottom half of the figure shows the resulting spatial distribution of primary

183 radiation damage when the microstructure is exposed to a typical pressurised
 184 water reactor (PWR) neutron flux. The particle and the matrix experience
 185 substantially different rates of damage when exposed to the same neutron
 186 flux. There is a distribution in damage in both phases approaching the in-
 187 terface, due to the transmission of PKAs between the phases.

188 In the case of W embedded in Al, the damage in W decreases near the
 189 edges of the particle, while the damage in Al increases near the interface. This
 190 can be explained by the fact that heavier W PKAs produce more damage
 191 than Al PKAs in the Al phase, and the inverse occurs in the W phase, where
 192 Al PKAs from the Al phase produce less damage than W PKAs. An inverted
 193 distribution is observed in the Fe/Mg system, where less damage is produced
 194 in the Mg particle compared to the Fe matrix, and a discontinuity is observed
 195 at the interface, with a minimum at the edge of the matrix and a maximum
 196 at the edge of the particle. This is due to self-screening effects discussed
 197 below.

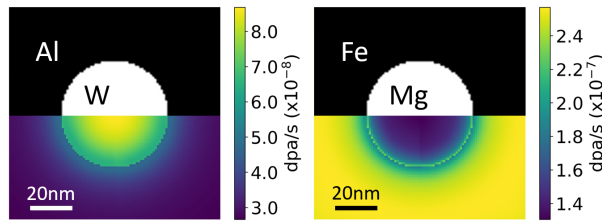


Figure 5: Example application of Eq. (1) to idealised microstructures containing a circular particle with radius 50 nm (white) in a matrix (black). Top half of each figure shows the microstructure, while the bottom half shows the resulting spatial distribution of dpa caused by a PWR neutron flux. (a) W particle in a Al matrix; (b) Mg particle in a Fe matrix.

198 *3.3. Application to a real alloy's microstructure*

199 Figure 6(a), modified from Teng et al. [27], shows a ferritic superalloy
200 which has an Fe matrix and NiAl secondary phase precipitates [28, 29]. The
201 phases of the superalloy contain both light (Al) and heavy (Fe/Ni) elements,
202 with similar thermal neutron scattering cross sections ($\sigma_{\text{Fe}} \approx 12 \text{ b}$, $\sigma_{\text{NiAl}} \approx$
203 10 b), slightly different atomic densities ($N_{\text{Fe}} = 8.5 \times 10^{22} \text{ cm}^{-3}$, $N_{\text{NiAl}} =$
204 $4.9 \times 10^{22} \text{ cm}^{-3}$) and the same threshold displacement energies ($E_{d\text{Fe}} = E_{d\text{NiAl}} =$
205 40 eV). Given the similar physical and nuclear properties of the two phases,
206 this system is an ideal candidate for the NRT assumptions of homogeneity.
207 However, our results show that the damage production, even in this system,
208 is far from homogeneous: figure 6 (b-d) shows the spatial distribution of pri-
209 mary radiation damage in the material calculated (b) using the NRT formula,
210 which assumes the material to be homogeneous, (c) treating each phase as
211 a bulk isolated material and applying NRT to each separately, and (d) with
212 our method, which explicitly accounts for microstructural complexity. A
213 common colour scale is used for figures (b-d).

214 The assumption of homogeneity is not applicable here, as it fails to cap-
215 ture the significant difference in radiation damage rate in the two phases —
216 up to 30% extra damage in the Fe matrix compared to the NiAl precipi-
217 tates. Interestingly, when the phases are treated in isolation (i.e. they are
218 assumed to be large enough that all damage is caused by PKAs generated
219 within the same phase), the results are qualitatively opposite to those of our
220 new method. This remarkable discrepancy is entirely explained by PKAs
221 travelling from one phase into the other, where they may be able to do more
222 or less damage per unit distance travelled, depending on their mass, kinetic

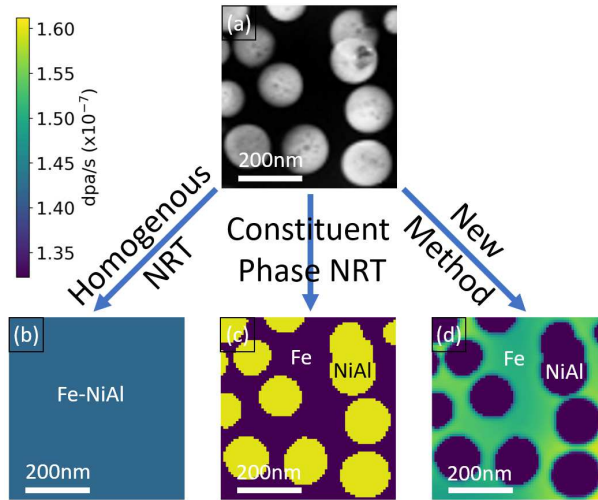


Figure 6: Spatial distribution of primary radiation damage in the ferritic superalloy due to a PWR flux. Top: TEM image modified from ref. [27] showing sample microstructure (light phase is NiAl, dark phase is ferrite). Bottom row shows the calculated dpa using: the NRT formula for a homogeneous mixture (left); the NRT formula of each phase separately (middle); our proposed method, which explicitly takes into account the microstructure (right).

223 energy and material's E_d .

224 To confirm that this is not an artifact of our method, but a new physical
 225 insight into the interplay of microstructure and primary radiation damage,
 226 we repeat the calculations on microstructures with increasingly larger grains
 227 (see Figure 7), which shows that our method converges to the results of the
 228 macroscopic approximation for sufficiently large particles (of order $100\ \mu\text{m}$
 229 in the case of Fe/NiAl). At some large length scale, most of the damage
 230 in a phase is produced by PKAs originating within the same phase, and so
 231 each phase can be treated separately as a bulk material as done previously
 232 [12], except for a thin boundary region near the interface. We find this as-

233 sumption holds when the particle diameter or grain size exceeds twice the
234 dominant PKA's range. However, if at least one of the phases is smaller,
235 the approximation of the independent bulk phases results in local under-
236 or over-estimation of the damage production rate, and may even affect the
237 macroscopic average damage production rate. This surprising finding cau-
238 tions against treating constituent phases of a material separately, as that can
239 be a worse approximation than assuming a homogeneous solid solution.

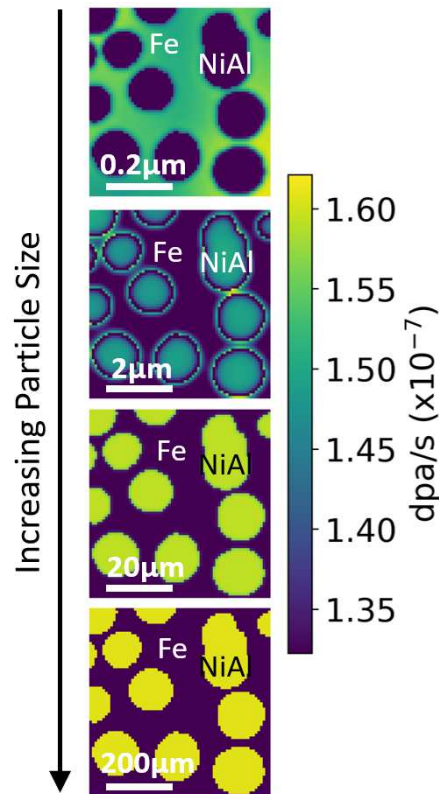


Figure 7: Spatial distribution of primary radiation in the ferritic superalloy at 4 different length scales. Note scale bar increase by one order of magnitude in each panel, while the colour scale is common throughout.

240 Our method also reveals that there is substantial variation within each

241 phase, as shown in figure 6(d). In the Fe matrix phase, regions surrounded
 242 by a high density of secondary phase receive substantially more damage than
 243 regions further away from precipitates. This difference is due to the effects
 244 of the microstructure on the PKA paths. The lighter Al PKAs generated
 245 within the NiAl phase, leave their phase of origin and approximately a third
 246 of the total ballistic energy is deposited in the matrix, as shown in Figure 8.
 247 Conversely, the heavier Fe and Ni PKAs remain localised to their origin phase
 248 and do not cause significant damage in the neighbouring phase.

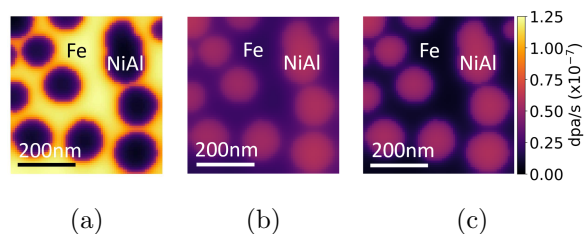


Figure 8: PKA species contributions to the total damage in Figure 6. (a): damage caused by Fe PKAs originating from the Fe matrix. (b) and (c): damage caused by Al and Ni PKAs, respectively, originating from the NiAl particles.

249 4. Discussion

250 The combined results of the previous section show that phase compo-
 251 sition and morphology of a microstructure have remarkable effects on the
 252 spatial distribution of primary radiation damage production. Importantly,
 253 this interplay between radiation damage production and microstructure is
 254 independent of any additional effects that interfaces may have on the re-
 255 combination of defects after they are produced. The latter is a well-studied
 256 phenomenon [30, 31, 32], which has driven the development of radiation

257 tolerant materials for the last decade [33, 34, 35]. In fact, the assumption
258 primary damage production cannot be controlled is so widespread that defect
259 recombination is often ascribed as the only contributing factor to radiation
260 tolerance of a material [30, 32]. However, in light of the current findings, it
261 is possible that in some cases part of the benefit of refined grain sizes lies in
262 a reduced defect production rate, as well as the well-documented enhanced
263 defect recombination rate.

264 This paper introduces a general framework to calculate the interplay
265 between microstructure and primary radiation damage distribution. This
266 framework is formally exact, but requires a prohibitive number of calcula-
267 tions (e.g. BCA simulations) to be applied to realistic microstructures. Thus,
268 we introduce a method to predicting the damage profile of a PKA as it crosses
269 an interfaces based solely on the PKA energy-damage profile of the parent
270 materials. The method was validated against explicit BCA calculations of
271 damage across planar interfaces, and was shown to produce accurate re-
272 sults, with $< 5\%$ root mean square error. This is remarkable considering the
273 computational saving of 6+ orders of magnitude. Specifically, calculations
274 such as Figure 6 are performed in the order of 100 cpu hr, while it would
275 take 5.4×10^9 cpu hr to obtain the same results through a large set of con-
276 ventional BCA simulations (see SI for calculation details), which is clearly
277 impracticable.

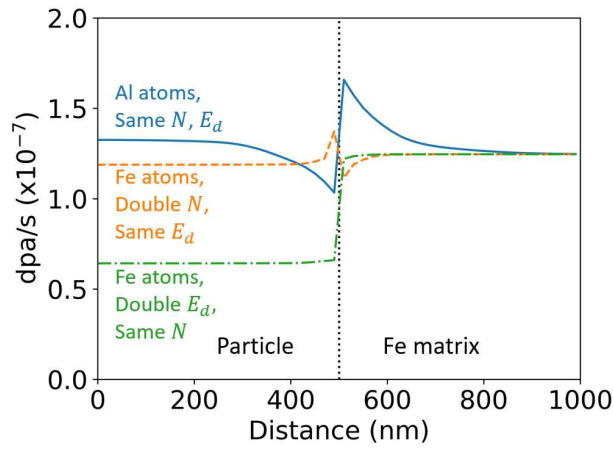
278 The computational speed-up, which is central to our method, becomes
279 even more remarkable in 3D volumes, and for 2D images that are larger
280 and/or have higher resolution than the ones presented here. The computa-
281 tional gains are chiefly due to the high-throughput approach to calculating

282 radiation damage across planar interfaces, which reduces the parameter space
283 of the BCA simulations that need to be run: simulations need only be run for
284 each PKA species and energy in the constituent materials. They do not need
285 to be run for all possible interface permutations that the PKA will encounter
286 — other than for validation purpose as shown in section 3.1. Additionally,
287 the data generated is used to create a library that can be reused for later
288 simulations. This makes our approach highly scalable, and it becomes pro-
289 gressively faster as more materials are added to the database.

290 The best accuracy in our benchmark is obtained when the interfaces are
291 very close or very far from the location where the PKA is produced. For
292 shallow interfaces, the collision cascade has not developed enough to alter
293 the profile in the post-interface material, resulting in minimal discrepancy.
294 For deep interfaces, most of the profile remains that of the initial material,
295 with minimal region afterwards in which a discrepancy can occur. For inter-
296 mediate interface depths, where the discrepancy is largest, it remains below
297 5% for all test cases. This provides an estimate for the uncertainty in the re-
298 sults, when the method is applied to 2D or 3D micro-structures. The results
299 shown in the previous section show local deviations in radiation damage rate
300 in the order of 30%, which is well above the uncertainty of the method.

301 A surprising insight from our method is that sometimes the primary ra-
302 diation damage exhibits a maxima and or minima on either or both sides of
303 an interface, while other times it results in a monotonic transition from one
304 phase to another. The behaviour depends on the combination of the chem-
305 ical species (specifically their cross-sections and atomic mass/charge), the
306 atomic density N and the threshold displacement energy E_d of the phases.

307 The relative contribution of each of those three variables is analysed in Fig-
 308 ure 9, which shows the damage distribution between a natural Fe matrix
 309 ($E_d = 40$ eV, $N = 8.49 \times 10^{22}$ cm $^{-3}$), and a particles of diameter 1 μ m made
 310 of a fictitious Fe-like material that shares the same material properties as true
 311 Fe except for one parameter: in one case (dashed orange line) the atomic den-
 312 sity N is doubled, in the second case (dot-dashed green line) E_d is doubled,
 313 and in the third case (solid blue line) the atomic mass and charge has been
 314 changed to that of Al (which has approximately half the mass and charge of
 315 Fe).



(a)

Figure 9: Cross-sectional profiles of damage through a 1 μ m diameter particle embedded in a natural Fe matrix. The particle is made of a fictitious Fe-like materials that comprises: Al atoms with the same N and E_d as Fe (solid blue line); Fe with double N and same E_d (dashed orange line); and Fe with double E_d and same N (dot-dashed green line).

316 Changing only E_d causes a proportional reduction in damage, with the
 317 material with double the E_d experiencing half the dpa, in agreement with the
 318 NRT formulation, and no other significant effect at the interface. When the

319 density is changed, a screening effect is observed. In the denser phase, the
320 PKAs cannot travel as far as they would in the less dense phase. Therefore
321 fewer particles originating from the denser phase can reach the less dense
322 side of the interface to cause damage. This results in a localised minimum
323 damage region in the less dense phase, and a localised maximum in the denser
324 phase. Far from the interface the profile has the same value, as the dpa in
325 homogeneous materials is independent of density, in agreement with NRT
326 theory. When the chemical species is changed, a similar screening effect is
327 seen. The range of a PKA is dependent on the mass and charge of the PKA,
328 with heavier and higher charged ions travelling shorter distances. As a result,
329 the phase with heavier constituent atoms plays the same role as the denser
330 material, and vice versa. The local maxima and minima are much more
331 pronounced in this case as both the mass and charge of Al are approximately
332 half that of Fe, both contributing to the PKA range, and hence screening
333 effect.

334 In a real material, combinations of the above effects will be observed.
335 This is further complicated by the fact that the damage experienced by each
336 phase will strongly depend on the nuclear cross sections of the isotopes in
337 both phases for the given flux. The cross sections determine how many
338 PKAs of each energy are produced and are available to cross the interface
339 and interact with the second phase, while also altering the amount of damage
340 experienced by the phase in which they originate. Importantly, considering
341 individual interface effects will not reveal *a-priori* how the effects will com-
342 bine at a given length scale, as evidenced in figure 6, and what will happen
343 when multiple secondary phases are in close proximity to each other with

344 overlapping interface effects.

345 Applying the new approach to real life alloys, we gain new physical insight
346 into the interplay between microstructure and radiation damage. Taking the
347 example of a ferritic superalloy designed for nuclear applications (ferrite with
348 NiAl precipitates of ~ 100 nm size), and exposing it to a typical PWR neutron
349 flux, we show that widely used assumption of homogeneity is inadequate, even
350 when the constituent phases have similar physical and neutronic properties
351 (such as Fe and NiAl). One finding obtained from the new method is that
352 performing NRT calculations on the constituent phases (i.e. treating them
353 as separate macroscopic phases) can lead to less accurate results than the
354 assumption of homogeneity. In the example of the ferritic superalloy, our
355 approach shows that the NiAl particles receive 30% less damage than the
356 surrounding ferrite matrix, which is the opposite of what is predicted by
357 NRT calculations carried out on phase separately as independent bulk phases.
358 More precisely, this is a relative error of -106% . The discrepancy is entirely
359 explained in terms of the transport of PKAs across phases: when a two-
360 phase microstructure is sufficiently refined, a substantial fraction of the total
361 damage is caused by PKAs that originate in another phase. This can lead to a
362 reduction in damage in one phase and an increase in another, or local changes
363 within a phase due to proximity to another phase. The key determining
364 factor for this effect is the length scale of the microstructure, compared to the
365 average range of the PKAs. In sufficiently large grains (approximately double
366 the average range of the PKAs) our results converge to those obtained from
367 NRT calculations of macroscopic bulk phases. However, for most modern
368 engineering alloys and composites, we caution against making assumptions of

369 homogeneity, or assuming (macroscopic) bulk phases; instead we recommend
370 using the novel method proposed above.

371 **5. Method**

372 *5.1. Computational details for neutron and BCA calculations*

373 All calculations were performed using a sample isotropic neutron flux for
374 the core of a pressurised water reactor (PWR) [36]. For each material consid-
375 ered, the resulting PKA fluxes were calculated using the `SPECTRA-PKA` code
376 [37], with a resolution of 2 logarithmically spaced bins per magnitude (see
377 supplementary information for neutron flux and convergence details).

378 BCA simulations were carried out using the `iradina` software [38], with
379 incident ion energy equal to the logarithmic mid point of the PKA bins.
380 For each BCA simulation, 10^5 ions were run. 100 equally spaced cells were
381 used, and the simulation length was set to 1.1 times the PKA range[9]. The
382 PKA energy-depth profile in a material is obtained by running a simulation
383 in the “Quick Calculation” mode and subtracting the energy deposited in
384 each cell (the sum of the electronic and ballistic energies) from the initial
385 PKA energy E_0 . The damage-depth profile is calculated using the method
386 developed by Stoller [14] and modified by Crocombette and Wambeke [39],
387 whereby the ballistic energy available for displacements obtained from “Full
388 Cascade” simulations is used in the NRT formula.

389 5.2. *Deterministic calculation of the spatial distribution of primary radiation*
 390 *damage*

The term S , F and f of Eq. (1) are detailed here. The source term S is

$$S(E) = \phi_{PKA}(\phi_N, E)N_sV \quad (2)$$

391 where the PKA flux, ϕ_{PKA} , is calculated from neutron cross-sections databases
 392 using SPECTRA-PKA [18, 19, 20] and N_s and V are the number density and
 393 volume of the source voxel, respectively. Voxels are cubic with side length p .

For an isotropic neutron flux, PKAs are generated isotropically, and a simple conservation argument can be used to determine the solid angle fraction, F^{3D} , of PKAs that a target voxel at a distance $|r - r_0|$ from the PKA source receives. In three dimensions, this is

$$F^{3D}(r_0) = \frac{p^2}{4\pi|r - r_0|^2} \quad (3)$$

where the area of the voxel that the sphere intersects is approximated as the square face of the voxel p^2 . In two dimensions voxels are equivalent to image pixels, and F becomes

$$F^{2D}(r_0) = \frac{p}{2\pi|r - r_0|} \quad (4)$$

394 In this formulation, there is no net loss/gain of PKAs by leaving/entering
 395 the plane of the image. Consideration about finite size effects are discussed
 396 below.

Finally, the PKA flux that interacts with the target voxel is converted into a damage rate through the function f , which combines the NRT theory with BCA results. Specifically,

$$f(r_0, E) = T \frac{p}{l} \frac{0.8}{2E_d(r)} \frac{1}{N_tV} \quad (5)$$

397 where the ballistic energy per ion T is deposited into each BCA cell of pre-
398 specified length l at location r . In the next section we outline how this energy
399 is calculated when the PKA crosses an interface. T is then normalised to the
400 size of the voxel, $\frac{p}{l}$, and used to calculate the number of atomic displacements
401 in each voxel following the NRT model. The last term converts this quantity
402 to dpa/s by dividing by the atomic density N_t and volume V of the target
403 voxel.

404 5.3. Analytical solution for the damage distribution across interfaces

The decay of an ion's kinetic energy through a material occurs in two regimes; a linear region due to electronic stopping, followed by a power law region due to nuclear stopping. This change in regimes occurs when the particle has a reduced LSS energy [21, 22, 23] of approximately $\epsilon_{LSS} = 0.3$ [26]. We produce analytical energy-depth profiles by fitting the average energy as a function of depth, $E(r)$, of a PKA with initial energy E_0 , to the function [26]

$$E(r) = \begin{cases} E_0 - mr & E(r) > \epsilon \\ A(d - r)^{1/c} & E(r) \leq \epsilon \end{cases} \quad (6)$$

where A , m and c are parameters. As the energy loss of the PKA must be smooth and continuous between the two regimes, m and A can be solved to give

$$m = \frac{E_0 - \epsilon}{d - (\epsilon/A)^c} \quad (7)$$

$$A = \left[\frac{\epsilon^c + c\epsilon^{c-1}(E_0 - \epsilon)}{d} \right]^{1/c} \quad (8)$$

where d , c and ϵ are fitting parameters. If the PKA is created with an energy that immediately places it within the nuclear stopping regime, $\epsilon = E_0$, and A further reduces to

$$A = \frac{E_0}{d^{1/c}} \quad \text{if } \epsilon = E_0 \quad (9)$$

The energy available for displacements is the sum of the PKA energy and the energy contained within the cascade particles. As a first order approximation, we assume that the spatial distribution of cascade particles, and the displacements they cause at a given location, is only dependent on the initial energy of the PKA, E_0 , and the current energy of the PKA at that location, E . The damage profile that a PKA generates in a second phase across an interface is therefore the same profile that an equivalent PKA would produce if it had originated from within the second phase with the same initial energy E_0 , and was offset such that the current PKA energy E was the same. We express the PKA ballistic energy available to cause damage, T , at a given distance r from the source as

$$T(E, r) = T_{\text{dam},r}(E) \quad (10)$$

where $T_{\text{dam},r}$ is the BCA average damage-energy profile of the specified PKA in the constituent material at location r , and is not explicitly dependent on the location of interfaces in a composite. However, T is implicitly dependent on the interface locations, as the energy at given distance from the source in a composite material is not known *a-priori* and must be found by using the average energy-depth profiles given in Eq. (6). The PKA energy is obtained by the function \mathcal{E}

$$E = \mathcal{E}(r, \mathbf{x}) \quad (11)$$

where \mathbf{x} is the array of interface locations. \mathcal{E} is a piecewise function such that before an interface the energy-depth profile is that of the first material, and after the interface, the energy-depth profile is that of the second material with the depth offset such the profile is continuous at the interface. For a series of layers (A, B, C, \dots) the ballistic energy can hence be expressed as

$$T(E, r) = T_{\text{dam},r}(\mathcal{E}(r, \mathbf{x})) \quad (12)$$

$$= \begin{cases} T_{\text{dam},A}(E_A(r)) & , 0 \leq r \leq x_1 \\ T_{\text{dam},B}(E_B(r + a_1)) & , x_1 < r \leq x_2 : E_A(x_1) = E_B(x_1 + a_1) \\ T_{\text{dam},C}(E_C(r + a_2)) & , x_2 < r \leq x_3 : E_B(x_2 + a_1) = E_C(x_2 + a_2) \\ \vdots & \vdots \\ \vdots & \vdots \end{cases} \quad (13)$$

405 5.4. Finite size effects

406 The damage produced in a target voxel is due to the sum of all PKAs
 407 originating in all neighbouring voxels within one PKA range, as described by
 408 Eq. (1) and Figure 1. As the simulation volume is necessarily finite, one must
 409 take into account the contribution of PKAs originating outside the simulation
 410 volume, to avoid an artificial reduction in damage near the simulation's edge.
 411 Several approaches exist to solve the problem either exactly or approximately,
 412 including the use periodic boundaries, reflective boundaries, tessellation and
 413 buffer layers.

414 For model microstructures, we partition the simulation volume into an
 415 inner region (the *window*) and a surrounding region (the *buffer*). Only the
 416 results of the window are shown here. Given that the the range of PKAs
 417 is known *a priori*, it is possible to counter the finite size effects entirely by
 418 using a buffer layer of width equal to maximum PKA range. In practice,

419 suitable convergence is obtained with substantially narrower buffer layers,
420 since the average PKA range is much lower than the maximum PKA range,
421 which is dominated by few PKAs with high energy (details in supplementary
422 information).

423 For real microstructures, we padded the region of interest with replicas
424 of the same image, flipped and tiled to ensure a continuous boundary at the
425 edge of the simulation. This effectively creates a fictitious but representative
426 volume of material to use as buffer, and in the limit of a large cell, it is
427 equivalent to applying reflective boundary conditions. Further details are
428 provided in the supplementary information.

429 **Data availability statement**

430 The data that support the findings of this study, beyond what is provided
431 in the supporting information, may be available from the corresponding au-
432 thor upon reasonable request.

433 **References**

- 434 [1] K. Nordlund, S. J. Zinkle, A. E. Sand, F. Granberg, R. S. Aver-
435 back, R. E. Stoller, T. Suzudo, L. Malerba, F. Banhart, W. J. Weber,
436 F. Willaime, S. L. Dudarev, D. Simeone, Primary radiation damage: A
437 review of current understanding and models, *Journal of Nuclear Mate-
438 rials* 512 (2018) 450–479. doi:10.1016/j.jnucmat.2018.10.027.
- 439 [2] B. Raj, M. Vijayalakshmi, Ferritic steels and advanced fer-
440 ritic–martensitic steels, in: *Comprehensive Nuclear Materials*, Elsevier,
441 2012, pp. 97–121. doi:10.1016/b978-0-08-056033-5.00066-5.

- 442 [3] S. Zinkle, Radiation-induced effects on microstructure, in: Comprehensive
443 Nuclear Materials, Elsevier, 2012, pp. 65–98. doi:10.1016/b978-0-
444 08-056033-5.00003-3.
- 445 [4] E. P. Wigner, Theoretical physics in the metallurgical labora-
446 tory of chicago, Journal of Applied Physics 17 (1946) 857–863.
447 doi:10.1063/1.1707653.
- 448 [5] G. H. Kinchin, R. S. Pease, The displacement of atoms in solids by radi-
449 ation, Reports on Progress in Physics 18 (1955) 1–51. doi:10.1088/0034-
450 4885/18/1/301.
- 451 [6] G. H. Kinchin, R. S. Pease, The mechanism of the irradiation disordering
452 of alloys, Journal of Nuclear Energy 1 (1955) 200–202. doi:10.1016/0891-
453 3919(54)90016-9.
- 454 [7] I. M. Torrens, M. T. Robinson, Computer simulation of atomic-
455 displacement cascades in solids in the binary-collision approximation,
456 Physical Review B 9 (1974) 5008. doi:10.1103/physrevb.9.5008.
- 457 [8] M. J. Norgett, M. T. Robinson, I. M. Torrens, A proposed method of
458 calculating displacement dose rates, Nuclear Engineering and Design 33
459 (1975) 50–54. doi:10.1016/0029-5493(75)90035-7.
- 460 [9] J. F. Ziegler, J. P. Biersack, The stopping and range of ions in mat-
461 ter, in: Treatise on Heavy-Ion Science, Springer US, 1985, pp. 93–129.
462 doi:10.1007/978-1-4615-8103-1.
- 463 [10] M. Gilbert, K. Arakawa, Z. Bergstrom, M. Caturla, S. Dudarev, F. Gao,
464 A. Goryaeva, S. Hu, X. Hu, R. Kurtz, A. Litnovsky, J. Marian, M.-C.

- 465 Marinica, E. Martinez, E. Marquis, D. Mason, B. Nguyen, P. Olsson,
466 Y. Osetskiy, D. Senior, W. Setyawan, M. Short, T. Suzudo, J. Trelewicz,
467 T. Tsuru, G. Was, B. Wirth, L. Yang, Y. Zhang, S. Zinkle, Perspectives
468 on multiscale modelling and experiments to accelerate materials
469 development for fusion, *Journal of Nuclear Materials* 554 (2021) 153113.
470 doi:10.1016/j.jnucmat.2021.153113.
- 471 [11] K. Nordlund, Historical review of computer simulation of radiation ef-
472 fects in materials, *Journal of Nuclear Materials* 520 (2019) 273–295.
473 doi:10.1016/j.jnucmat.2019.04.028.
- 474 [12] A. Adrych-Brunning, M. R. Gilbert, J.-C. Sublet, A. Harte, C. P.
475 Race, Modelling the interaction of primary irradiation damage
476 and precipitates: Implications for experimental irradiation of zir-
477 conium alloys, *Journal of Nuclear Materials* 498 (2018) 282–289.
478 doi:10.1016/j.jnucmat.2017.10.022.
- 479 [13] J. F. Ziegler, SRIM-2003, *Nuclear Instruments and Methods in Physics*
480 *Research Section B: Beam Interactions with Materials and Atoms* 219-
481 220 (2004) 1027–1036. doi:10.1016/j.nimb.2004.01.208.
- 482 [14] R. Stoller, M. Toloczko, G. Was, A. Certain, S. Dwaraknath, F. Gar-
483 ner, On the use of SRIM for computing radiation damage expo-
484 sure, *Nuclear Instruments and Methods in Physics Research Section*
485 *B: Beam Interactions with Materials and Atoms* 310 (2013) 75–80.
486 doi:10.1016/j.nimb.2013.05.008.
- 487 [15] M. T. Robinson, Computer simulation studies of high-energy collision

- 488 cascades, Nuclear Instruments and Methods in Physics Research Section
489 B: Beam Interactions with Materials and Atoms 67 (1992) 396–400.
490 doi:10.1016/0168-583x(92)95839-j.
- 491 [16] R. Smith, Atomic and Ion Collisions in Solids and at Surfaces, Cam-
492 bridge University Press, 2005.
- 493 [17] ASTM-International, Astm e521-16, standard practice for investigating
494 the effects of neutron radiation damage using charged-particle irradiation
495 (2016). doi:10.1520/e0521-16.
- 496 [18] M. R. Gilbert, J. Marian, J.-C. Sublet, Energy spectra of primary knock-
497 on atoms under neutron irradiation, Journal of Nuclear Materials 467
498 (2015) 121–134. doi:10.1016/j.jnucmat.2015.09.023.
- 499 [19] M. R. Gilbert, J.-C. Sublet, Pka distributions: Contributions from trans-
500 mutation products and from radioactive decay, Nuclear Materials and
501 Energy 9 (2016) 576–580. doi:10.1016/j.nme.2016.02.006.
- 502 [20] M. R. Gilbert, J.-C. Sublet, Differential dpa calculations with
503 spectra-pka, Journal of Nuclear Materials 504 (2018) 101–108.
504 doi:10.1016/j.jnucmat.2018.03.032.
- 505 [21] J. Lindhard, V. Nielsen, M. Scharff, Integral equations governing radi-
506 ation effects, Matematisk-fysiske Meddelelser udgivet af Det Kongelige
507 Danske Videnskabernes Selskab 33 (1963).
- 508 [22] J. Lindhard, M. Scharff, H. E. Schiott, Range concepts and heavy
509 ion ranges, Matematisk-fysiske Meddelelser udgivet af Det Kongelige
510 Danske Videnskabernes Selskab 33 (1963).

- 511 [23] J. Lindhard, V. Nielsen, M. Scharff, Approximation method in classical
512 scattering by screened coulomb fields, *Matematisk-fysiske Meddelelser*
513 udgivet af Det Kongelige Danske Videnskabernes Selskab 36 (1968) 1–
514 31.
- 515 [24] A. Mohammadi, S. Hamidi, M. A. Asadabad, The use of the
516 SRIM code for calculation of radiation damage induced by neu-
517 trons, *Nuclear Instruments and Methods in Physics Research Section*
518 *B: Beam Interactions with Materials and Atoms* 412 (2017) 19–27.
519 doi:10.1016/j.nimb.2017.08.036.
- 520 [25] U. Saha, K. Devan, S. Ganesan, A study to compute integrated dpa for
521 neutron and ion irradiation environments using SRIM-2013, *Journal of*
522 *Nuclear Materials* 503 (2018) 30–41. doi:10.1016/j.jnucmat.2018.02.039.
- 523 [26] K. B. Winterbon, P. Sigmund, J. B. Sanders, Spatial distribution of
524 energy deposited by atomic particles in elastic collisions, *Matematisk-*
525 *fysiske Meddelelser udgivet af Det Kongelige Danske Videnskabernes*
526 *Selskab* 37 (1970) 5–70.
- 527 [27] Z. K. Teng, M. K. Miller, G. Ghosh, C. T. Liu, S. Huang, K. F.
528 Russell, M. E. Fine, P. K. Liaw, Characterization of nanoscale
529 NiAl-type precipitates in a ferritic steel by electron microscopy
530 and atom probe tomography, *Scripta Materialia* 63 (2010) 61–64.
531 doi:10.1016/j.scriptamat.2010.03.013.
- 532 [28] S. Huang, G. Ghosh, X. Li, J. Ilavsky, Z. Teng, P. K. Liaw, Effect of
533 al on the NiAl-type b2 precipitates in ferritic superalloys, *Metallurgical*

- 534 and Materials Transactions A 43 (2012) 3423–3427. doi:10.1007/s11661-
535 012-1318-y.
- 536 [29] G. Song, Z. Sun, L. Li, X. Xu, M. Rawlings, C. H. Liebscher, B. Clausen,
537 J. Poplawsky, D. N. Leonard, S. Huang, Z. Teng, C. T. Liu, M. D. Asta,
538 Y. Gao, D. C. Dunand, G. Ghosh, M. Chen, M. E. Fine, P. K. Liaw,
539 Ferritic alloys with extreme creep resistance via coherent hierarchical
540 precipitates, *Scientific Reports* 5 (2015) 16327. doi:10.1038/srep16327.
- 541 [30] G. Odette, M. Alinger, B. Wirth, Recent developments in irradiation-
542 resistant steels, *Annual Review of Materials Research* 38 (2008) 471–503.
543 doi:10.1146/annurev.matsci.38.060407.130315.
- 544 [31] G. Ackland, Controlling radiation damage, *Science* 327 (2010) 1587–
545 1588. doi:10.1126/science.1188088.
- 546 [32] X.-M. Bai, A. F. Voter, R. G. Hoagland, M. Nastasi, B. P.
547 Uberuaga, Efficient annealing of radiation damage near grain
548 boundaries via interstitial emission, *Science* 327 (2010) 1631–1634.
549 doi:10.1126/science.1183723.
- 550 [33] I. Beyerlein, A. Caro, M. Demkowicz, N. Mara, A. Misra, B. Uberuaga,
551 Radiation damage tolerant nanomaterials, *Materials Today* 16 (2013)
552 443–449. doi:10.1016/j.mattod.2013.10.019.
- 553 [34] M. J. Demkowicz, P. Bellon, B. D. Wirth, Atomic-scale design of
554 radiation-tolerant nanocomposites, *MRS Bulletin* 35 (2010) 992–998.
555 doi:10.1557/mrs2010.704.

- 556 [35] W. Han, M. J. Demkowicz, N. A. Mara, E. Fu, S. Sinha, A. D. Rollett,
557 Y. Wang, J. S. Carpenter, I. J. Beyerlein, A. Misra, Design of radia-
558 tion tolerant materials via interface engineering, *Advanced Materials* 25
559 (2013) 6975–6979. doi:10.1002/adma.201303400.
- 560 [36] FISPACT-II, Reference input spectra (2018).
561 URL https://fispact.ukaea.uk/wiki/Reference_input_spectra
- 562 [37] M. R. Gilbert, Spectra-pka is available as a utility within fispact-ii and
563 now also available to download from github at. (2018).
564 URL <https://github.com/fispact/SPECTRA-PKA>
- 565 [38] C. Borschel, C. Ronning, Ion beam irradiation of nanostructures –
566 a 3d monte carlo simulation code, *Nuclear Instruments and Methods*
567 *in Physics Research Section B: Beam Interactions with Materials and*
568 *Atoms* 269 (2011) 2133–2138. doi:10.1016/j.nimb.2011.07.004.
- 569 [39] J.-P. Crocombette, C. V. Wambeke, Quick calculation of damage for ion
570 irradiation: implementation in iradina and comparisons to SRIM, *EPJ*
571 *Nuclear Sciences & Technologies* 5 (2019) 7. doi:10.1051/epjn/2019003.

572 **Acknowledgements**

573 This research was supported by an Australian Government Research
574 Training Program (RTP) Scholarships. MIB acknowledges the Tyree foun-
575 dation for financial support through a philanthropic Tyree UNSW nuclear
576 engineering scholarship.

577 **Author information**

578 M.I. Brand (first author) performed all the calculations, data analysis,
579 and theory implementation, and drafted the manuscript. O.G. Obbard con-
580 tributed through insightful discussion, interpretation of the data and provid-
581 ing computational hardware. P.A. Burr (corresponding author) contributed
582 to conception, supervision, computational design and financial support. All
583 authors contributed to editing the manuscript.

584 **Competing interests**

585 The authors declare no competing interests.

Supplementary Files

This is a list of supplementary files associated with this preprint. Click to download.

- [SI2.pdf](#)